JOURNAL OF GEOPHYSICAL RESEARCH, VOL. 104, NO. B5, PAGES 10,421–10,437, MAY 10, 1999

Quantifying tectonic strain and magmatic accretion at a slow spreading ridge segment, Mid-Atlantic Ridge, 29°N

J. Escartín,[1,2,3] P. A. Cowie,[2] R. C. Searle,[1] S. Allerton,[2,4]
N. C. Mitchell,[1,5] C. J. MacLeod,[6] and A. P. Slootweg[1]

Abstract. High-resolution, deep-towed side-scan sonar data are used to characterize faulting and variations in tectonic strain along a segment of the slow spreading Mid-Atlantic Ridge near 29°N. Sonar data allow us to identify individual fault scarps, to measure fault widths and spacing, and to calculate horizontal fault displacements (heave) and tectonic strain. We find that over long periods of time (>1 Myr on average), tectonic strain is ~10% on average and does not vary significantly along axis. There is a marked asymmetry in tectonic strain that appears to be linked to asymmetric accretion along the whole segment, indicated by ~50% lower tectonic strain on the east flank than on the west flank. These variations in tectonic strain do not correlate directly with changes in fault spacing and heave. Fault spacing and heave increase from the center of the segment toward the end (inside corner) on the west flank and from the outside to the inside corner across the axis. These parameters remain relatively constant along the segment on the east flank and across the axis at the segment center. Tectonic strain appears to be decoupled from magmatic accretion at timescales >1 Myr, as the decrease in magma supply from the segment center toward the end (inferred from variations in crustal thickness along the axis) is not correlated with a complementary increase in tectonic strain. Instead, tectonic strain remains relatively constant along the axis at ~7% on the east flank and at ~15% on the west flank. These results indicate that variations in fault development and geometry may reflect spatial differences in the rheology of the lithosphere and not changes in tectonic strain or magma supply along axis.

1. Introduction

The structure of the oceanic crust and seafloor morphology are the result of magmatic accretion (i.e., dike injection, gabbroic intrusions) and extensional processes (i.e., brittle faulting, ductile deformation) taking place at mid-ocean ridges (MORs). The relative importance of extensional faulting appears to increase with decreasing spreading rate, as indicated by changes in size of fault-generated abyssal hills [e.g., *Goff et al.*, 1997], or analyses of fault populations at fast and slow spreading ridges [e.g., *Edwards et al.*, 1991; *Carbotte and Macdonald*, 1994]. It has also been proposed that changes in lithospheric thickness [e.g., *Forsyth*, 1992; *Shaw*, 1992], rheology [e.g., *Escartín et al.*, 1997b] or magma supply [e.g., *Laughton et al.*, 1979; *Searle and Laughton*, 1981; *Searle et al.*, 1988b] also control the style of faulting at MORs.

Detailed study of a slow spreading ridge may provide constraints on the effect of each of these parameters on faulting. From marine geophysical and geological studies and modeling results it has been proposed that melt supply [e.g., *Kuo and Forsyth*, 1988; *Lin et al.*, 1990; *Detrick et al.*, 1995], lithospheric thickness [e.g., *Parmentier and Forsyth*, 1985; *Shaw and Lin*, 1996], and crustal composition [e.g., *Cannat et al.*, 1995] change systematically from segment centers towards the ends. It has been hypothesized that variation in melt supply may be linked directly to tectonic strain [e.g., *Alexander and Macdonald*, 1996], which would result in increased tectonic strain from the segment center towards the ends, where melt supply is reduced [e.g., *Jaroslow*, 1996; *Allerton et al.*, 1996]. Either increased lithospheric thickness or reduced fault strength due to serpentinization can result in strain localization favoring the formation of large faults widely spaced at the end of segments [*Francis*, 1981; *Forsyth*, 1992; *Shaw*, 1992; *Shaw and Lin*, 1996; *Escartín et al.*, 1997b], independently of variations in tectonic strain along the ridge axis. It is thus necessary to determine if observed variations in fault patterns are linked to changes in tectonic strain.

In addition to along-axis variations in fault geometry (i.e., fault spacing and throw) and magmatic supply along a ridge segment, there is also a marked asymmetry across the ridge axis of slow spreading ridges. The inside corners (ICs) of ridge-offset discontinuities are characterized by elevated terrain and thin crust with respect to the outside corners (OCs) or segment centers (SCs) [e.g., *Severinghaus and Macdonald*, 1988; *Tucholke and Lin*, 1994; *Escartín and Lin*, 1995] and frequently contain outcrops of serpentinized peridotite [*Cannat*, 1993; *Tucholke and Lin*, 1994; *Cannat et al.*, 1995]. At ICs, faults are also more irregular, larger, and more widely spaced than at SCs or OCs [*Tucholke and Lin*, 1994; *Cannat et al.*, 1995; *Escartín and Lin*, 1995; *Jaroslow*, 1996]. According to *Jaroslow* [1996], tectonic strain estimated from multibeam bathymetry may be ~50% larger

[1]Department of Geological Sciences, University of Durham, Durham, England.
[2]Department of Geology and Geophysics, University of Edinburgh, The Grant Institute, Edinburgh, Scotland.
[3]Now at Laboratoire de Pétrologie, Université Pierre et Marie Curie, Paris, France
[4]Now at Robertson Research International, Llandudno, Wales.
[5]Now at Department of Earth Sciences, University of Oxford, Oxford, England.
[6]Department of Earth Sciences, University of Wales, Cardiff, Wales.

Paper number 1998JB900097.
0148-0227/99/1998JB900097$09.00

at the IC than at the OC or SC. However, the differences in the average tectonic strain between the segment center and end (both IC and OC) are small and vary among the three Mid-Atlantic Ridge (MAR) segments studied [*Jaroslow*, 1996]. This variability among segments suggests that the effects of magma supply, lithospheric thickness, or rheology on faulting are poorly understood and require further investigation. In particular, careful characterization of fault patterns and quantification of tectonic strain along a slow spreading segment can provide additional constraints on these controls.

Tectonic strain along a ridge segment is accommodated near the surface by the nucleation, linkage and growth of faults in the brittle domain [e.g., *Alexander and Macdonald*, 1996]. At slow spreading ridges, faults initiated within the axial valley floor are short and have small throws, and some develop into large faults along the rift-valley walls [*McAllister and Cann*, 1996]. Faults may remain active at distances of up to ~15-35 km from the ridge axis, as indicated by the width of the seismically active zone [e.g., *Lin and Bergman*, 1990; *Wolfe et al.*, 1995]. Studies that quantify the proportion of the total plate separation accommodated by brittle deformation at MORs are scarce and are based on a wide variety of datasets. Estimates of tectonic strain at the slow spreading MAR vary between ~18% (high-resolution bathymetry, 37°N [*Macdonald and Luyendyk*, 1977]), 10-20% (teleseismic earthquakes [*Solomon et al.*, 1988]), ~25% (high-resolution side-scan sonar, 24°N [*Allerton et al*, 1996]), and >30% (multibeam bathymetry and HMR1 side-scan sonar data, 27-28°N [*Jaroslow*, 1996]). This disparity of estimates may arise from differences in the methods used to calculate faulting strain, in addition to possible regional or local variations in strain. The spatial resolution of ~100 m of sea surface multibeam bathymetry data makes them unsuitable to properly characterize small-scale faulting (faults with lengths <2 km and displacements <200 m), and estimates based on such data may be inaccurate [e.g., *Cowie et al.*, 1994].

The deep-towed side-scan sonar from the Towed-Ocean Bottom Instrument (TOBI) provides high-resolution sonar imagery (~10 m spatial resolution), which allows us to characterize both large- and small-scale faulting. The data presented here were collected on board RRS *Charles Darwin* (see *Searle et al.* [1998a] for cruise details). Sonar data covered the southern two thirds of a slow spreading ridge segment at the northern MAR (29°N), extending to ~40 km off axis (~2.8 Ma old crust), with a track spacing of ~2 km (Figure 1). This survey geometry pro-

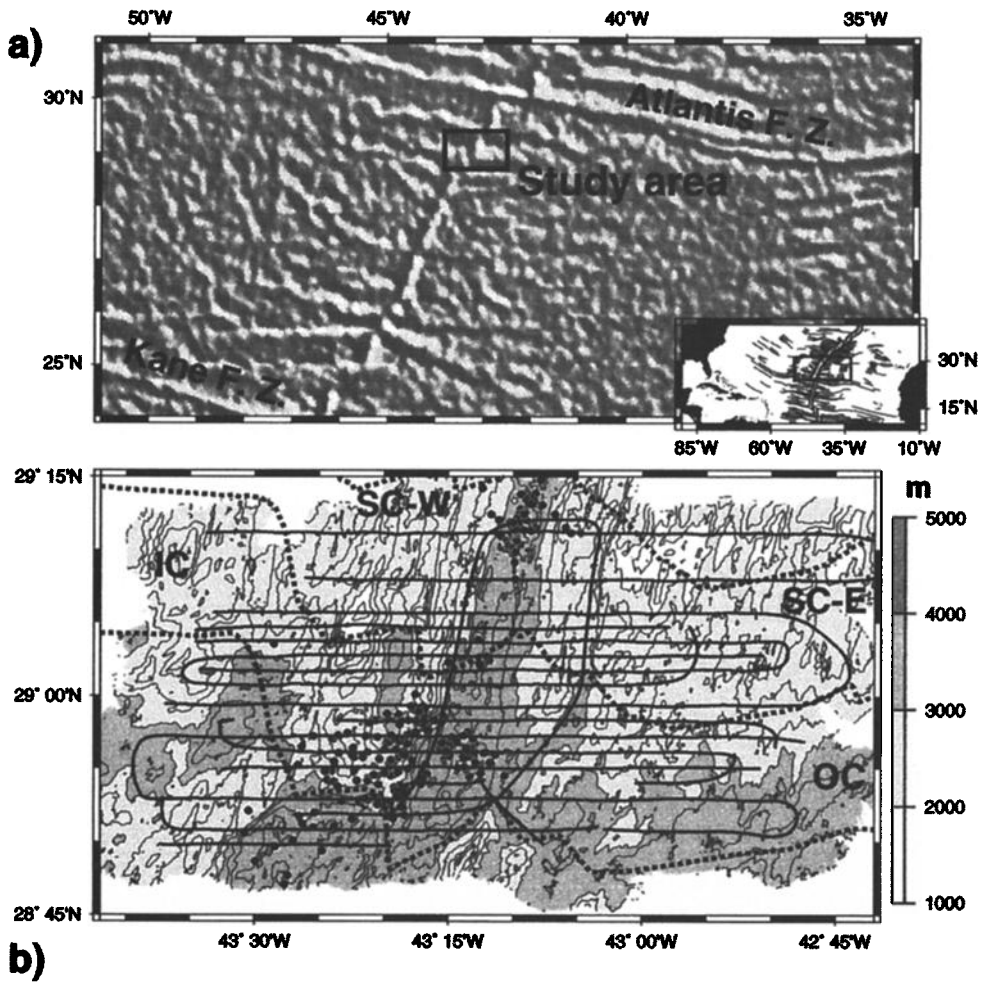

Figure 1. (a) Illuminated satellite gravity map [*Sandwell and Smith*, 1993] of the Mid-Atlantic Ridge between the Atlantis and Kane Fracture Zones showing location of the study area. Inset shows location of the map in the northern Atlantic (traces of transform and non-transform discontinuities from *Escartín* [1996]). (b) Multibeam bathymetric map of the study area (100-m grid spacing, 250-m contours). Continuous lines correspond to the TOBI tracks, and the dashed lines to the boundaries between different tectonic regions. IC, inside corner; SC-W, segment center, West flank; SC-E, segment center, East flank; OC, outside corner. The locations of microseismic epicenters from *Wolfe et al.* [1995] are also shown (circles).

vides ~100% sonar coverage of the area and allows us to better understand geometry of seafloor structures with the two opposite looking directions that are available (north and south looking, Figure 1). Previous studies using TOBI or similar deep-towed instruments have covered the axial valley floor in detail [e.g., *Macdonald and Luyendyk*, 1977; *Kong et al.*, 1988; *McAllister et al.*, 1995; *Smith et al.*, 1995; *McAllister and Cann*, 1996; *Allerton et al*, 1996], but data over ridge flanks and away from the ridge axis have been scant [e.g., *Macdonald and Luyendyk*, 1977]. This segment has also been the focus of several geological and geophysical studies in the past [e.g., *Lin et al.*, 1990; *Purdy et al.*, 1990; *Shaw*, 1992; *Rommeveaux et al.*, 1994; *Sempéré et al*, 1993, 1995; *Murton et al.*, 1995; *Pariso et al.*, 1995; *Smith et al.*, 1995], which provide information to constrain variations in crustal thickness, melt supply, thermal structure, and crustal composition along the segment.

TOBI side-scan sonar data allow us (1) to obtain strain estimates based on high-resolution fault interpretations, and (2) to determine how tectonic strain is coupled with melt supply along the axis. Tectonic strain, fault spacing, and horizontal fault displacement (heave) estimates, as well as their spatial variations, are obtained from the interpreted fault maps. These data are compared with existing models of crustal accretion at slow spreading ridges to constrain the relationship between melt supply and tectonic strain.

2. Tectonic setting

The study focuses on the second MAR segment south of the Atlantis Fracture Zone, bounded by the 29°23'N and 28°51'N nontransform discontinuities [*Sempéré et al.*, 1993] (Figure 1a). The present full spreading rate is ~26 mm/yr [e.g., *Sempéré et al.*, 1995], but plate separation is highly asymmetrical, with >60% of the total plate separation occurring on the east flank [*Allerton*, 1997; *Searle et al.*, 1998a]. The morphology of the rift valley is typical of a slow spreading ridge segment, with a narrow and shallow valley at the center that widens and deepens towards the discontinuities (Figure 1b). This segment has been the site of several geophysical studies in the past that have described its morphology [*Purdy et al.*, 1990; *Sempéré et al.*, 1993; 1995; *Shaw*, 1992; *Smith et al.*, 1995], gravity and crustal structure [*Lin et al.*, 1990; *Rommeveaux et al.*, 1994], and tectonic evolution [*Searle et al.*, 1998a]. The crust is thicker at the SC and OC than at the IC [*Rommeveaux et al.*, 1994], possibly reflecting the combined effect of focused magmatic accretion on-axis [e.g., *Kuo and Forsyth*, 1988; *Lin et al.*, 1990] and tectonic thinning at ICs [*Escartín and Lin*, 1995]. The IC terrain is characterized by larger faults (>1 km in throw) than at the the OC or SC (<0.5 km) [*Shaw*, 1992; *Shaw and Lin*, 1993] and by diffuse microseismic activity [*Wolfe et al.*, 1995] (Figure 1b).

Traces of the nontransform discontinuities bounding the segment to the north and south, as inferred from existing bathymetry [*Rommeveaux et al.*, 1994] and satellite altimetry data [*Escartín*, 1996], demonstrate that the offsets have migrated along the axis with time. To compare faulting patterns and tectonic strain in different parts of the segment, we have divided the segment into three zones (north, center, and south). The north-center and center-south boundaries correspond to one third and two thirds of the distance between the two bounding discontinuities in a direction parallel to the ridge axis (~010°). Our data cover mainly the center and south sections of the segment. To study spatial variability in faulting and tectonic strain we have separated these sections across the axis into IC and OC (segment end) and SC-E and SC-W (segment center, Figure 1b).

3. Data Description

TOBI deep-towed side-scan sonar operates at 30 kHz and has a scan width of ~6 km when operated at 400-600 m from the seafloor. The average spatial resolution at this towing altitude is ~10 m (for more details on instrument specifications, see *Flewellen et al.* [1993] and *le Bas et al.* [1995]). The TOBI tracklines were oriented E-W and spaced ~2 km apart (Figure 1b; see *Searle et al.* [1998a] for cruise details). This survey geometry provided almost 100% overlap of backscatter data between adjacent lines in most of the survey area, which allowed us to obtain almost complete north- and south-looking side-scan sonar mosaics (Plates 1 and 2). The use of mosaics with uniform looking direction facilitates the identification of tectonic features across TOBI tracks, and the availability of two looking directions helps to constrain the geometry of these features.

The backscatter data were processed for noise reduction, slant range, and gain corrections using the methods described by *le Bas et al.* [1995]. The data were then located geographically using estimates of the TOBI position and the attitude of the vehicle (heading, pitch, and roll), projected onto a horizontal plane below the vehicle. TOBI navigation was calculated from the ship's position, length of wire out, and depth of TOBI using our modification [*CD99 Scientific Party*, 1996] of *Hussenoeder et al.*'s [1995] implementation of *Triantafyllou and Hover*'s [1990] cable-modeling algorithm. The processed and remapped data were separated into north and south looking to create two digital mosaics in each of the main directions of insonification (north and south, Plates 1 and 2, respectively).

4. Fault Identification and Analysis

Quantification of tectonic strain accommodated by brittle processes requires spatial identification of faults and their geometry, and measurement of both fault displacement (vertical or horizontal) and spacing. Faults are identified in the side-scan sonar data as zones of relatively strong backscatter intensity, with high length to width ratios and characteristic tectonic (i.e., linear [*McAllister and Cann*, 1996; *Searle et al.*, 1998a]) rather than magmatic texture (i.e., hummocky terrain, shingled areas [*Smith et al.*, 1995]). Backscatter intensity depends on insonification direction, fault geometry, and grazing angle, in addition to the acoustic reflectivity of the seafloor. Thus large variability in backscatter is expected for different faults across the study area. The use of images with two insonification directions provides in most cases sufficient information to determine if a high-backscatter area does correspond to a steep scarp, and if so, to constrain its geometry and orientation. Examples of identified faults for four small areas of the digital mosaics are shown in Figure 2, corresponding to the IC, OC and SC (east and west). Only those scarps positively identified as fault-related have been digitized to create the fault map in Figure 3, and used in the fault analysis described below. Fault analysis has been performed along E-W transects spaced every 0.5 km (Figure 4), which allows us to calculate tectonic strain without relying on empirical length-displacement scaling relationships for faults [see *Dawers et al.*, 1993; *Cowie et al.*, 1994].

Larger faults identified in the backscatter mosaics are in good agreement with steep scarps as identified in the multibeam bathymetric maps (Figure 5). The west wall of the rift valley in

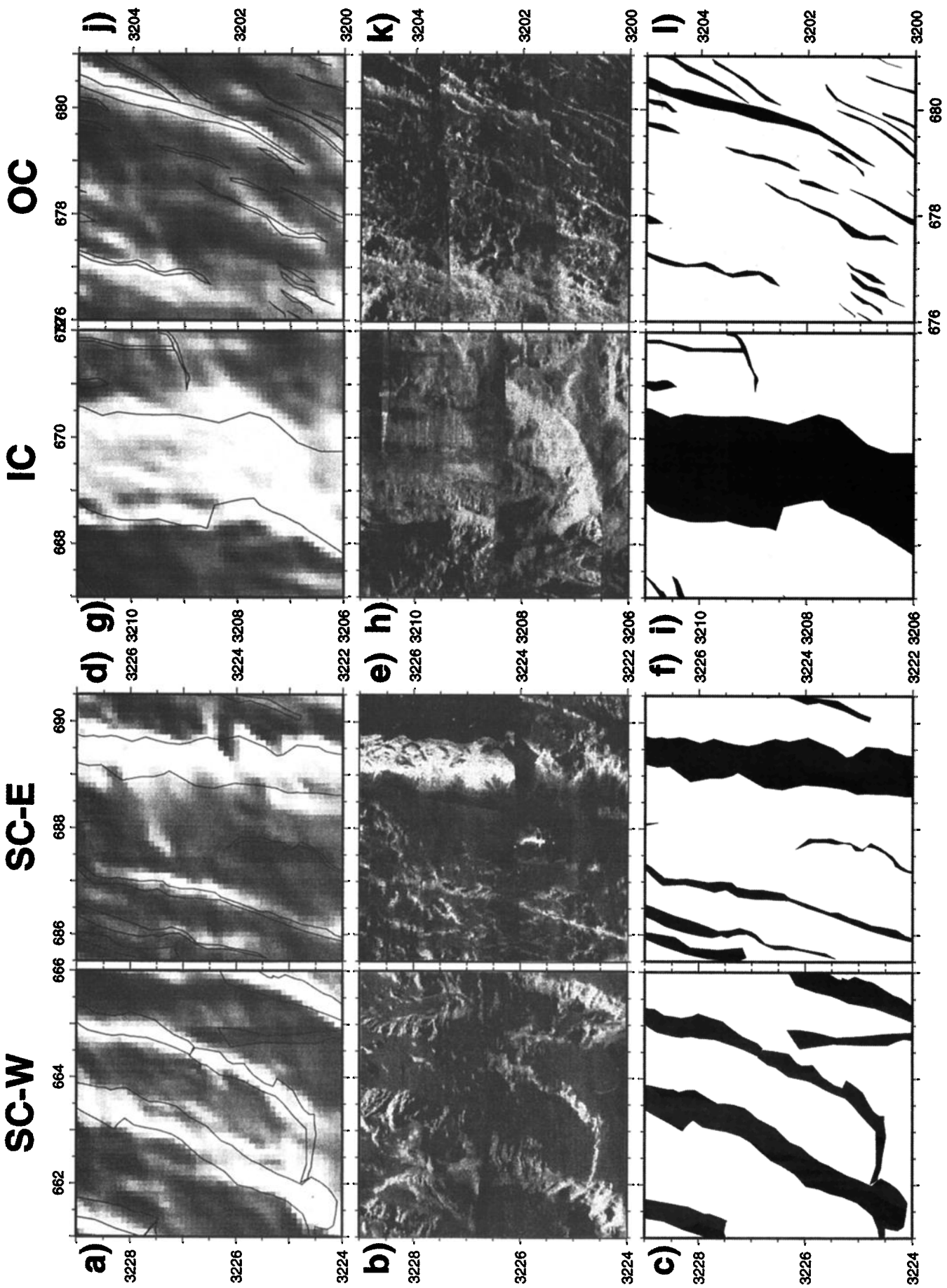
SC-W
SC-E
IC
OC
a)
b)
c)
d) g)
e) h)
f) i)
j)
k)
l)
3228
3226
3224
3226 3210
3224 3208
3222 3206
3204
3202
3200
662
664
666
686
688
690
668
670
676
678
680

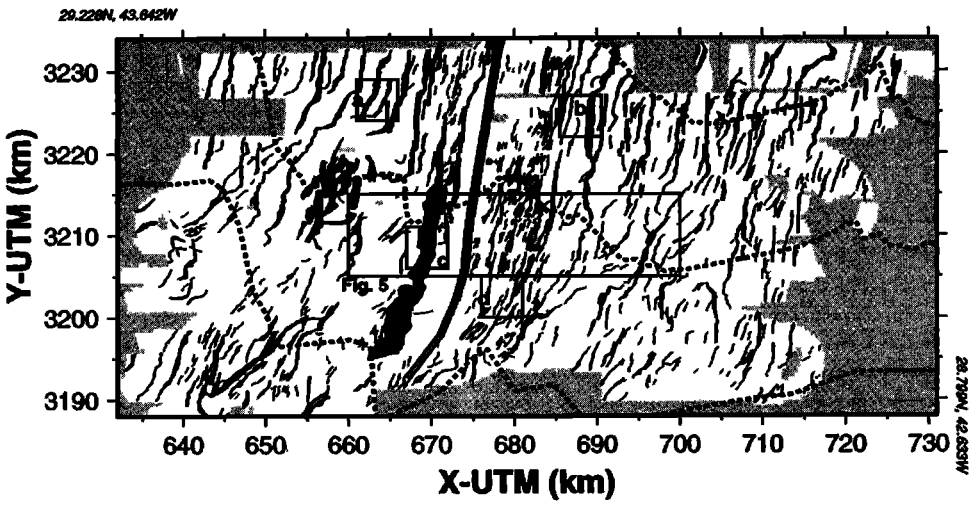

Figure 3. Fault map interpreted from the digital side-scan sonar mosaics. Inward facing faults are marked in black, and outward facing faults by outlined gray areas (see also Figure 4). The ridge axis is indicated by the double line, and the dashed gray lines correspond to the southern nontransform discontinuity and to the boundaries between the defined tectonic regions (see Figure 1). Underlying squares mark the location of the four areas shown in Figure 2 (a; SC-W, b; SC-E, c; IC, d; OC) and that of Figure 5.

the south corresponds to the largest identified fault scarp (Plate 1 and Figure 3) with >1000m of vertical relief (Figure 1). The width of the fault as identified on the sonar data is in good agreement with that identified from the multibeam bathymetry (Figure 5a). In other areas (east flank, e.g., Figure 5, X=697 km), bathymetric scarps correspond to several faults interpreted from the backscatter, which have small heave (<500 m) and are closely spaced (<1 km). These smaller faults are not resolved by the multibeam bathymetry.

To accurately quantify tectonic strain and magmatic accretion, we have determine the polarity of faults (inward versus outward facing faults, Table 1), measure their spacing and heave (Tables 2 and 3), and calculate tectonic strain (Table 4).

4.1. Fault Facing Direction

We determine for each fault whether the orientation of the fault scarp is toward the ridge axis or away from it (inward and outward facing faults, respectively, Figure 3 and Table 1). As most of the faults are subparallel to the ridge axis, with very few subperpendicular to it, this distinction is unambiguous in most cases if both the north and south looking backscatter mosaics are used in the interpretation (Plates 1 and 2).

4.2. Fault heave *h*

The width of a digitized fault (Figure 3) in the E-W direction is assumed to correspond to the horizontal component of displacement of the fault, or fault heave h. The E-W transects are only 10° off the spreading direction (~100° from NUVEL-1 plate model [*DeMets et al.*, 1990]). Assuming that fault displacement is mostly downdip extensional with no substantial strike-slip component, the error of the observed or apparent (h^*) versus the real heave (h) parallel to spreading (100°) is <3% and therefore negligible.

A potentially more important source of error may arise from the interpretation of the bright backscatter units as representative of the real heave. In some cases these bright areas may include highly reflective talus built up by mass wasting at the base of the fault [*Allerton et al.*, 1996], and the measured heave will then correspond to an "apparent heave." The difference between the apparent and the real heave will depend on the dip of the fault, talus slope, proportion of the fault height covered by the talus, and erosion of the fault scarp by mass wasting (scarp retreat), among other parameters and processes. Talus slopes measured from near-bottom bathymetry available in an adjacent area of the northern MAR [*Tucholke et al.*, 1997; *Goff and Tucholke*, 1997] yield values as high as 35°. Assuming a talus angle of 30° covering ~40% of an uneroded fault scarp, we can estimate that h can be 60% or equal to h^* for dips of fault equal to 60° or 30°, respectively (Figure 6a). A dip of fault equal to ~45°, consistent with dips estimated from earthquake focal mechanisms [*Thatcher and Hill*, 1995] and high-resolution bathymetry [*Macdonald and Luyendyk*, 1977; *Tucholke et al.*, 1997; *Goff and Tucholke*, 1997], would give h=0.8 h^*. Any mass wasting resulting in fault scarp retreat may also make h^* larger than h (Figure 6b). Other processes such as partial burial of the fault scarp by lava flows [e.g., *Macdonald et al.*, 1996] may result in a reduction of h^* instead.

Figure 2. Comparison of (top) illuminated multibeam bathymetry, (middle) side-scan sonar data, and (bottom) detailed fault interpretation for selected areas corresponding to the (a-c) SC-W, (d-f) SC-E, (g-i) IC, and (j-l) OC. The outline of digitized faults is also shown on the shaded relief maps for comparison (100 m grid, Figure 1b). Backscatter data for the areas in the west flank (SC-W and IC, b and h) correspond to the south looking mosaic (Plate 1), while data for areas on the east flank (SC-E and OC, e and k) correspond to south looking mosaic (Plate 2). Locations of these areas are indicated on the fault map in Figure 3. We note that the fault map (bottom) is interpreted from both northward and southward looking mosaics (see Figure 3), but for each area the backscatter image is shown for only one of the looking directions.

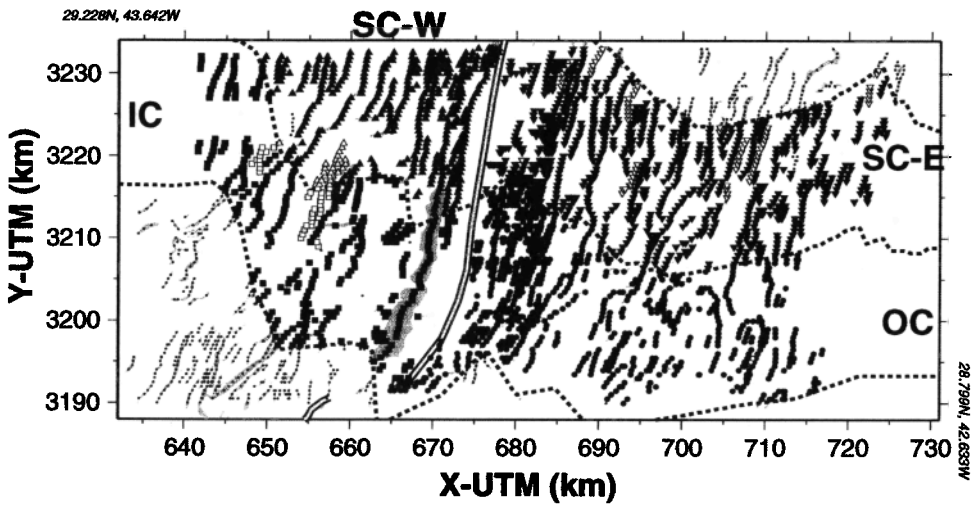

Figure 4. Location of fault measurements along E-W transects used in the fault and strain analysis. The location of each fault measurement is indicated by solid or open symbols (inward and outward facing faults, respectively). Fault analysis has only been done for the southern inside corner (IC, squares) and outside corner (OC, circles) and the segment center at the east and west flanks (SC-E and SC-W, triangles and inverted triangles) of the 29°N segment (bigger symbols); faults corresponding to the segment immediately to the south and to the segment end toward the north (smaller symbols) have not been used in the analyses.

In this study we assume that fault and talus geometry throughout the study area do not vary, and therefore we use apparent heave to provide an upper bound of the tectonic strain and to estimate its spatial variability. Determination of slope of the talus ramp requires high-resolution, near-bottom bathymetry that is not available for all our survey area. Processes that may affect the estimates of fault heave, such as scarp retreat or burial of fault scarps by lava flows, are not well characterized in this area and are out of the scope of this paper. Lacking any additional constraints, we assume that these processes are self-similar and do not vary spatially. Such assumption is implied in studies that use backscatter data to estimate strain [e.g., *Cowie et al.*, 1993]. In Table 2 we report the average and corresponding standard deviation of measured (apparent) fault heaves for all areas, calculated for all the faults and for the inward and outward facing populations (see Figures 7a and 7b).

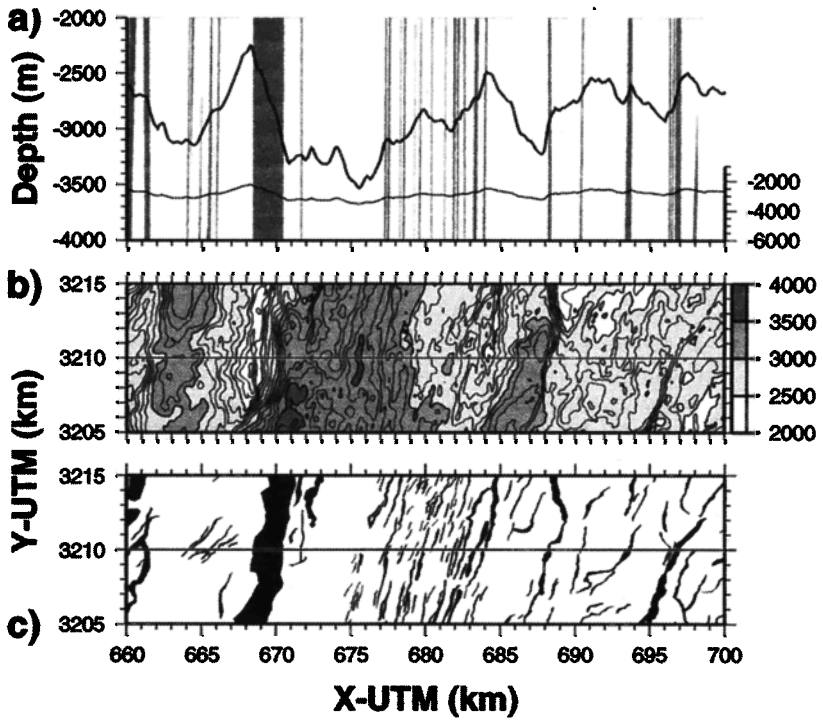

Figure 5. (a) Comparison of interpreted fault scarps (gray bars) from the backscatter data with multibeam bathymetry data. The bathymetric profile is shown both with vertical (8×) and no vertical exaggeration (thick and thin lines, respectively). (b) Location of the bathymetric profile in Figure 5a on a relief map of the area (100 m-contours). (c) Faults interpreted from the backscatter data (see location in Figure 3) for the same area as in Figure 5b.

Table 1. Number and Percentage of Inward and Ourward Facing Faults

	N_a	N_i	N_o
All	3119	2934 (94.1)	170 (5.6)
SC-W	520	486 (93.5)	28 (5.4)
SC-E	1082	1004 (92.8)	71 (6.6)
IC	411	373 (90.8)	36 (8.8)
OC	958	955 (99.7)	3 (0 3)

N_a:, total number of faults along transects (Figure 4). N_i, number of inward facing faults. N_o, number of outward facing faults. Values in parentheses are percentages.

4.3 Fault spacing *s*

Fault spacing *s* is measured from the separation between centers of adjacent faults along E-W transects (Figures 4, 7c and 7d) or from the length (*L*) of the transects extending to the edge of the bacscatter data divided by the number of faults along it (*N/L*, Table 3). Estimates of fault spacing based on number of faults per unit length are systematically lower than the transect averages (Table 3), as the portions at the end of each transect with no faults are included in the calculation. In all cases the average fault spacing and corresponding standard deviation are given. As discussed below, fault populations (heave and spacing) do not follow Gaussian distributions, so in both cases we report the standard deviation instead of the standard error, as this first parameter may be more indicative of the variability in fault parameters than the second one.

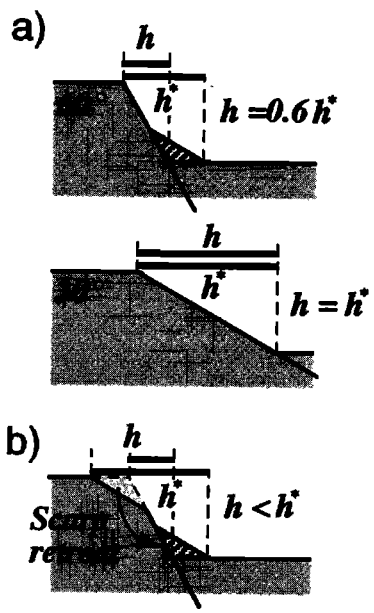

Figure 6. Illustration of some of the possible errors associated with estimates of fault heave from backscatter data. (a) Variations in fault geometry (dip of the fault) and talus. The observed fault heave (h^*) may include talus in addition to the actual fault surface, and therefore may overestimate the real fault heave (h). Error will depend on the relative height of the scarp covered by the talus, on the angle of the talus, and on the angle of the fault. (b) Mass wasting can also result in retreat of the fault scarp, giving apparent heaves that are larger than the real heave.

4.4. Tectonic strain, ε

Tectonic strain estimates given in Table 4 are calculated from the measured fault heave and spacing using three different methods: (1) from the mean values of *h* and *s* along each of the transects (Figures 4 and 7), (2) from the slopes of the cumulative fault heave plots (*m*, Figure 8), and (3) from the cumulative fault heave along each transect divided by the length of the transect ($\Sigma h/L$). These different estimates are given to determine the variability in tectonic strain depending on the method used.

In the following we refer to "apparent heave" as "heave" and to "apparent tectonic strain" as "tectonic strain," unless otherwise noted. Fault height cannot be measured directly as extensive high-resolution, deep-towed bathymetry data are not available, and smaller faults identifiable on the backscatter data cannot be recognized on the shipboard multibeam data (see Figure 5). If dip of fault, talus angle, and relative height of the talus are constant throughout the area, fault heave may be used as a proxy for fault height (see Figure 6).

Analyses of *s*, *h* and ε have been carried out for each of the tectonic provinces (SC-W, SC-E, IC, and OC, Figure 1), as well as for the whole fault population, and for inward and outward facing faults (Figures 3 and 4). The subscripts *a*, *i*, and *o* are used to refer to all, inward and outward facing fault populations (see Tables 2-4). Those faults with unclear facing direction (single, sharp acoustic reflection in both looking directions) were used only in the analyses which included all the faults and were disregarded in the analyses which treated inward and outward facing faults separately.

5. Results of Fault and Strain Analyses

5.1. Inward Versus Outward Facing Faults

Almost all of the faults identified from side-scan sonar data are inward facing (Figures 2 and 5), with <6% of the total number of faults being outward facing (Table 1). The largest concentration of outward facing faults is found at the west flank of the IC (~9%), while they are almost non-existent at the OC (<0.5%). Differences across the axis at the SC are not significant (~6.6% at the SC-E, ~5.5% at the SC-W). Multibeam bathymetry reveals numerous steep slopes facing away from the axis. These areas show backscatter textures typical of sedimented volcanic morphologies (i.e., hummocky terrain and seamounts [*Smith et al*, 1995]), with no evidence for bright and linear reflectors expected for outward facing faults, and are therefore interpreted as back-tilted volcanic terrain. Earlier studies along the MAR indicate that outward facing faults are not very common [*Macdonald and Luyendyk*, 1977; *Searle and Laughton*, 1981;

Table 2. Fault Heave Parameters

	$\overline{h_a}$	$\overline{h_i}$	$\overline{h_o}$
All	197 (293)	193 (296)	270 (233)
SC-W	257 (278)	252 (272)	384 (385)
SC-E	154 (146)	151 (147)	204 (108)
IC	412 (618)	420 (641)	354 (293)
OC	107 (103)	107 (103)	259 (41)

In meters. $\overline{ha}$, $\overline{hi}$, and $\overline{ho}$ correspond to the average heave and the standard deviation (in parentheses) for all, inward, and outward facing faults, respectively.

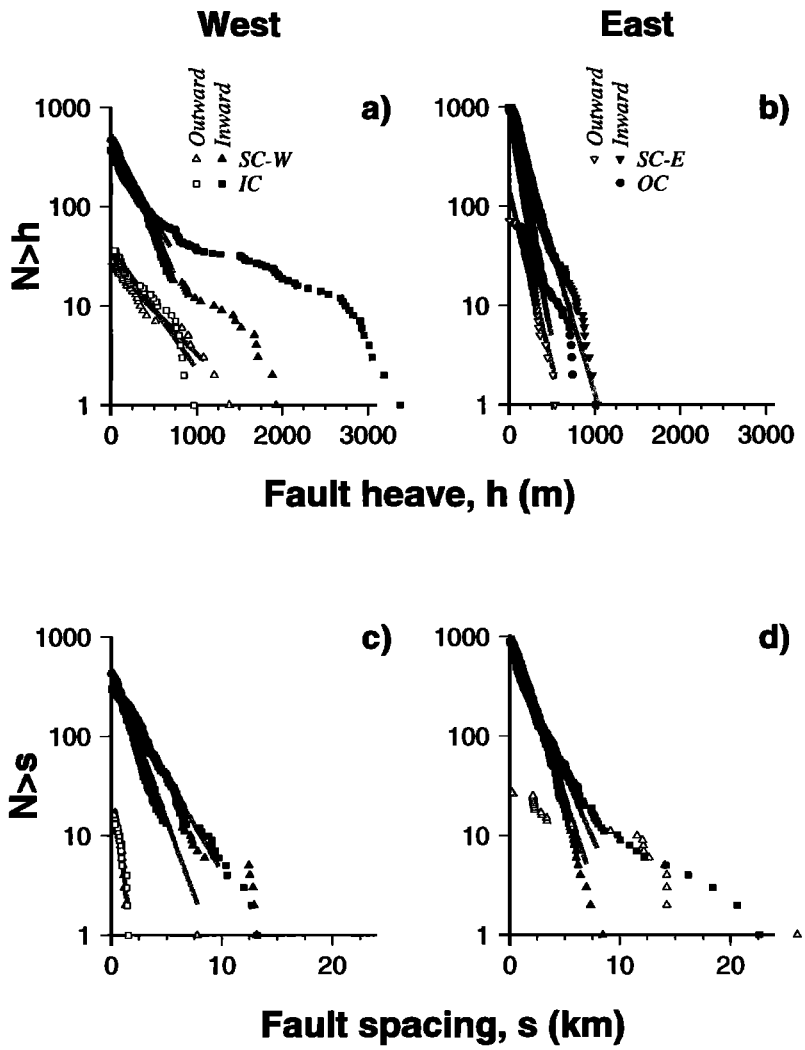

Figure 7. Log-linear plots of the distributions of (a-b) fault heave h and (c-d) spacing s for the different tectonic environments (same symbol conventions as in Figure 4). Only the populations of inward (solid symbols) and outward facing faults (open symbols) are shown. The shaded lines correspond to best fit of an exponential function to the data; the fit of the function has only been done to the portion of the data that show a linear distribution in the plot (see text). Note the marked asymmetry in the slopes of the distributions from west to east (left and right) and the absence of outward-facing faults at the outside corner. Mean fault heave and spacing estimates are given in Tables 2 and 3.

Kong et al., 1988], although *Jaroslow* [1996] reports that up to 40% of the faults are outward facing.

5.2. Fault Population Statistics

Cumulative size-frequency distributions of fault parameters have often been used to characterize fault populations [e.g., *Carbotte and Macdonald*, 1994; *Cowie et al.*, 1994]. The cumulative distributions of h and s at the IC, SC (east and west), and OC terrain (Figure 8) show that at $s < 9$ km and $h < 500$ m, the populations can be fitted with an exponential distribution (shaded lines in Figure 7) of the type

$$N(h,s)=N_T e^{-\lambda h,s}$$

Table 3. Fault Spacing Parameters

	$\overline{s_a}$	$\overline{s_i}$	$\overline{s_o}$	L/N_a	L/N_i	L/N_o
All	1.77 (1.77)	1.70 (1.87)	4.64 (6.62)	1.87 (1.28)	2.10 (1.51)	0.48 (1.51)
SC-W	1.53 (1.41)	1.54 (1.73)	1.20 (1.77)	1.60 (0.64)	1.77 (0.71)	5.95 (3.74)
SC-E	1.40 (1.16)	1.50 (1.28)	7.20 (6.34)	1.51 (0.64)	1.74 (0.94)	6.16 (6.23)
IC	2.59 (2.06)	2.69 (2.22)	0.96 (0.36)	2.44 (1.35)	2.62 (1.35)	5.78 (2.76)
OC	1.55 (2.09)	1.55 (2.09)	-	1.70 (1.67)	1.71 (1.67)	-

In kilometers. $\overline{s_a}$, $\overline{s_i}$, and $\overline{s_o}$ correspond to the average fault spacing and the standard deviation (in parentheses) for each area. L/N corresponds to the transect length (L) divided by the total number of faults (N) along a transect. Values are given for all faults, inward, and outward facing faults, respectively.

Table 4. Tectonic Strain (%)

	$\overline{h}/\overline{s}$			m			$\Sigma h/L$		
	ε_a	ε_i	ε_o	ε_a	ε_i	ε_o	ε_a	ε_i	ε_o
All	11.5 (5.7)	10.7 (5.1)	0.8 (1.4)	10.6 (5.9)	9.9 (5.0)	0.7 (1.5)	10.53	9.19	2.58
SC-W	16.6 (7.2)	15.1 (6 8)	1.4 (2.9)	17.0 (7.7)	15.8 (7.4)	1.2 (2.7)	16.06	14.23	6.45
SC-E	8.0 (3.1)	7.2 (2.8)	0.8 (0.8)	8.9 (3.2)	8.3 (3.0)	0.6 (0.8)	10.19	8.67	1.26
IC	14.8 (6.0)	14.0 (5.4)	0.8 (2.2)	10.2 (5.9)	9.7 (4.8)	0.5 (1.8)	16.88	16.00	6.12
OC	6.8 (3.1)	6.8 (3.1)	(0)	7.3 (3.5)	7.3 (3.5)	(0)	6.29	6.26	(0)

Estimates of tectonic strain (ε) from average heave and spacing, $\overline{h}/\overline{s}$, from slopes of cumulative fault heave m (Figure 8), and from the cumulative fault heave and transect length $\Sigma h/L$. Numbers in parentheses correspond to the standard deviations. In all cases, strain is calculated for all faults (ε_a), inward-facing faults (ε_i), and outward facing faults (ε_o).

where $N(h,s)$ is the number of faults with heave (h) or spacing (s) larger than a given value of h or s, and N_T is the total number of faults. The reciprocal of λ is the characteristic value of h or s, which should correspond to the mean of h or s if the population is properly characterized by an exponential distribution. At higher values of s and h ($s > 9$ km and $h > 500$ m) the cumulative distribution cannot be described satisfactorily by this simple population model. Consequently, fault spacing and heave have been quantified using the mean values of h and s instead of the characteristic values ($1/\lambda$) of the corresponding exponential distributions.

5.2.1. Variations in fault heave. Fault heave estimates show significant variations among the different tectonic environments (Table 2). Fault heave at the IC is largest ($\overline{h_a}$~400 m), while that at the OC is smallest ($\overline{h_a}$~100 m). The SC-W and SC-E fault populations show intermediate fault heaves compared to those of

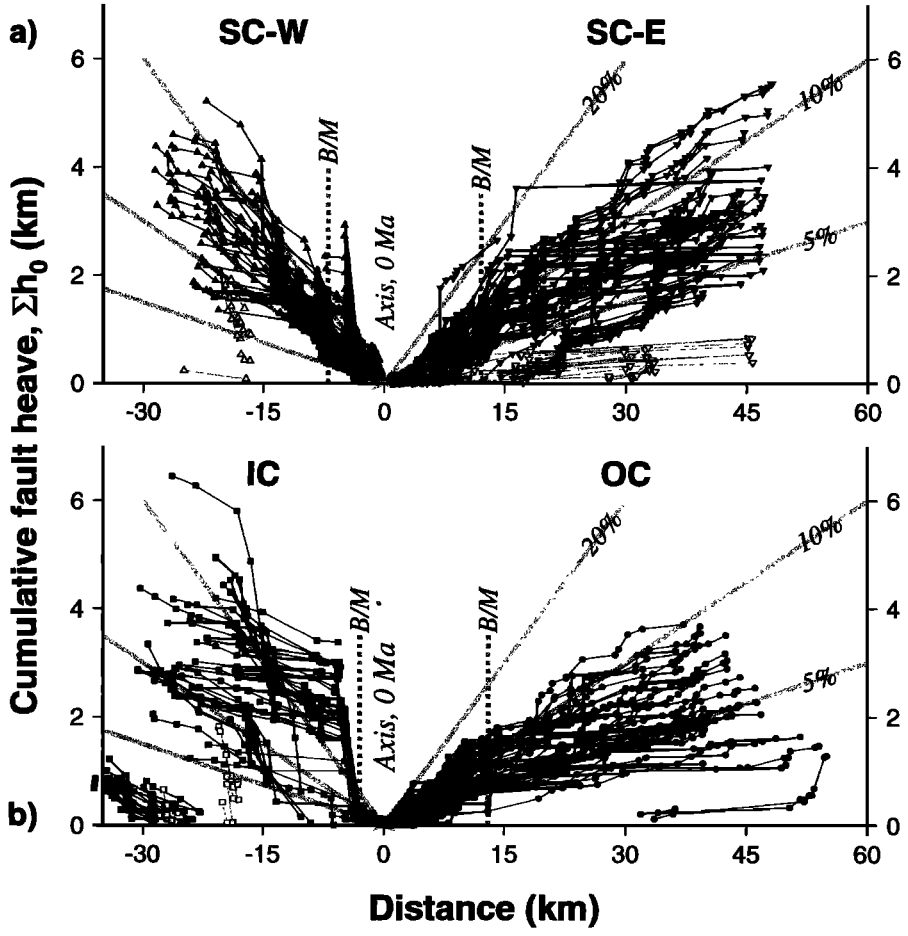

Figure 8. Plot of cumulative fault heave Σh_0 versus distance from the axis for all the transects (see Figure 4) for the segment (a) center and (b) end. Both inward and outward facing Σh_0 lines are shown (solid and open symbols, respectively). Shaded lines corresponding to 5% and 10% strain are plotted for reference. Note the marked east-west asymmetry in the overall slope of the curves, even at the segment center. The smallest amount of strain occurs at the OC, while the largest is found at the IC. Same symbol convention has been used as in Figures 4 and 7. The dashed shaded lines labeled B/M mark the edges of the central magnetic anomaly (Brhunes-Matuyama boundary). There is a clear asymmetry about the axis, with <40% total accretion taking place on the west flank than on the east flank [*Allerton*, 1997].

the IC and OC, but there is a marked asymmetry; faults tend to be larger on the west flank ($\overline{h_a}$~250 m) than on the east flank ($\overline{h_a}$~150 m), similar to the asymmetry observed at the end of the segment (compare IC and OC, Table 2).

5.2.2. Variations in fault spacing. Fault spacing is estimated from the average of measured spacings s, and from the length of the transect divided by the total number of faults along each transect (L/N, Table 3). Owing to the small number of outward facing faults and to their clustering, particularly on the west flank (Figure 4), the average of measured spacing is lower than that estimated from the number of faults per unit length (e.g., at the IC, $\overline{s_o}$=0.96 km, L/N_o=5.8 km). Discrepancies are smaller in the estimates of spacing for inward-facing and for all faults (Table 3), as they are more abundant and evenly distributed across the area (Figure 4).

Faults are more widely spaced at the IC ($\overline{s_a}$=2.59 km) than in the other tectonic provinces (Table 3). There is some asymmetry at the segment end, with the spacing at the OC ($\overline{s_a}$=1.55 km) similar to that of the SC-E ($\overline{s_a}$=1.40 km) and SC-W ($\overline{s_a}$=1.53 km). No significant asymmetry is observed at the SC (Table 3). In all cases, average fault spacings are smaller than the 1-1.4 km estimated from similar fault studies in the fast spreading East Pacific Rise [*Edwards et al.*, 1991].

5.3. Tectonic Strain Estimates

Tectonic strain and its spatial variation are estimated from the measured fault parameters h and s (Tables 2 and 3), and from the cumulative fault heave along transects (Figure 8). These estimates of tectonic strain are apparent and not absolute (being based on apparent and not absolute heave), but they provide an upper bound to actual tectonic strain. In Table 4 the estimates of the average tectonic strain for each of the tectonic provinces are given. Fault heave is measured along transects spaced 0.5 km apart (Figure 4), thus adequately characterizing the displacement of faults <1.5 km in length. Using typical displacement-length scaling relationships [e.g., *Cowie and Scholz*, 1992; *Dawers et al.*, 1993], faults with a length of ~1.5 km would have displacements of the order of ~15 m, well below the resolution of any shipboard multibeam system. This suggests that scaling laws inferred from continental areas need to be calibrated before being applied to the oceanic environment.

Average tectonic strain for the study area is found to be ε_a~11% (Table 4), depending on the method used, although locally it can be larger than 20% (see slopes in Figure 8), qualitatively in agreement with results from earlier studies [e.g., *Macdonald and Luyendyk*, 1977; *Solomon et al.*, 1988; *Allerton et al*, 1996; *Jaroslow*, 1996]. Strain accommodated by outward facing faults is typically <3%, while that accommodated by inward facing faults is >9% (Table 4). There is a marked asymmetry east-west across the axis both at the segment center and end (Figure 8), indicated by tectonic strains on the west flank which are a factor of 2 greater than on the east flank. While the OC shows the smallest tectonic strain (~6-7%), the strain at the IC is similar to that at the SC-W (~11-17% and 16-17%, respectively, Table 4). The average tectonic strain decreases slightly from ~12-13% at the segment center to ~9-12% at the segment end, depending on the strain estimate used. We consider that these along-axis variations in tectonic strain are not significant tectonically given that there is some variability depending on the method used in the estimation; in all cases we report the maximum and minimum estimates of the tectonic strain (see Table 4).

The spatial variations of fault spacing, fault heave and tectonic strain at 29°N are summarized in in Figure 9. In this sketch we use values for one of the estimates of fault spacing, fault heave and tectonic strain, but similar patterns would arise if other estimates given in Tables 2-4 were used instead.

6. Discussion

6.1. Fault Formation and Zone of Active Deformation

Variations in fault spacing and heave with distance from the ridge axis allow us to constrain the zone of active tectonic deformation where faults form, develop, and remain active. *McAllister and Cann* [1996], based on TOBI data from the axial valley floor of this segment, suggested that faults are formed and linked within a "fault growth window." According to this model this "window" extends along the whole length of the segment and has a width of a few kilometers beginning at ~2 km from the neovolcanic zone. However, our analysis of the fault data demonstrates that this model may be valid only in some sections of the segment studied. Plates 1 and 2 and Figure 3 show a marked near-axis asymmetry in fault spacing, heave, and overall fault patterns that suggests significant variability in the scale and nature of strain localization.

Constraints on the lateral extent of active faulting may be obtained from microsesimic activity and the backscatter character of the sonar data. Microseismic activity over a period of 41 days reported by *Wolfe et al.* [1995] extends to ~10 km off axis at the segment end and is restricted to the median valley at the segment center (Figure 1b). These data are likely to give a minimum estimate of the width of the active zone due to the limited recording time. Fault patterns and backscatter character may provide instead constraints fault formation and evolution at geological timescales (~1 Myr). Examination of the fault patterns in Plates 1 and 2 and Figure 3 reveals: (1) a lack of faults near the ridge axis (within ~2 km), (2) a well-developed zone ~10 km wide of small-scale faulting (fault lengths <5 km and s<0.5 km) on the east flank along the whole segment, and (3) a less developed ~5-km-wide zone of small-scale faulting at the segment center on the west flank that disappears toward the segment end (IC). The zone of recent, unsedimented volcanics (high reflectivity area in

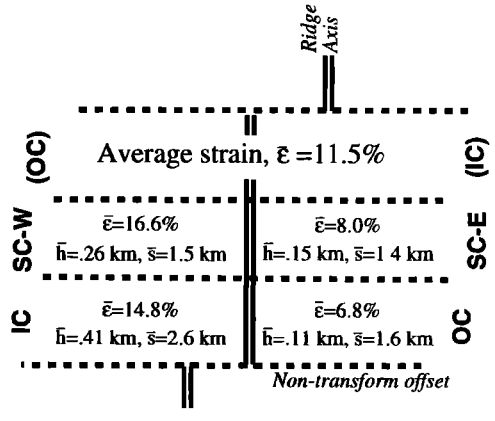

Figure 9. Sketch showing the spatial variation in fault heave, fault spacing, and tectonic strain along the studied segment. The nontransform offsets and the limit among zones (dashed lines) are shown horizontal for simplicity (see Figure 1). Values reported correspond to the average heave including all the faults (Table 2), average of measured spacing (Table 3), and the strain estimated from average spacing and heave along transects (Table 4). The same overall spatial variations are observed if other estimates of fault spacing (Table 3) or tectonic strain (Table 4) are used instead.

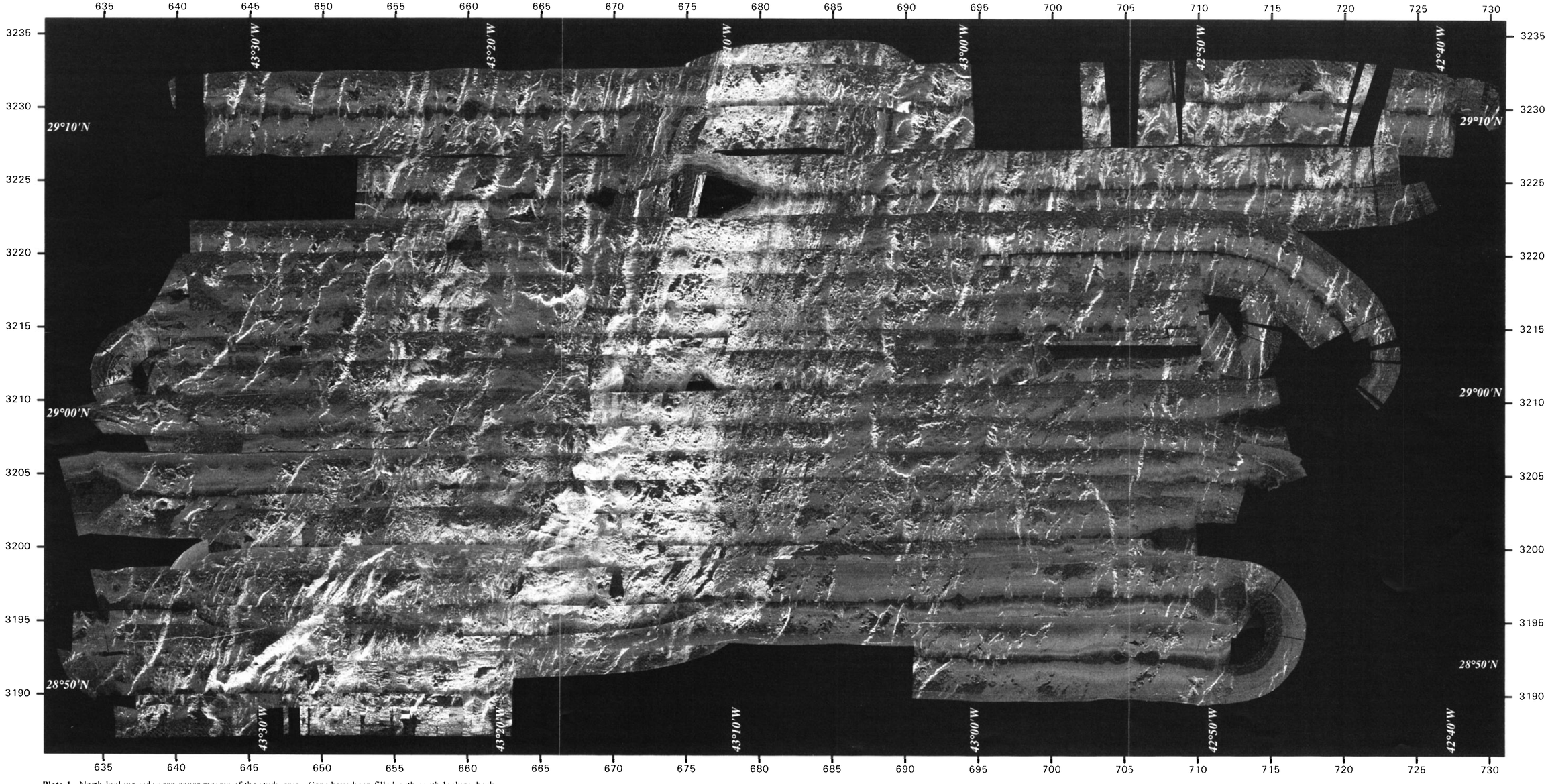

Plate 1. North-looking side-scan sonar mosaic of the study area. Gaps have been filled with south-looking backscatter data (Plate 2). Coordinates are both in UTM (km, black) and latitude/longitude (white).

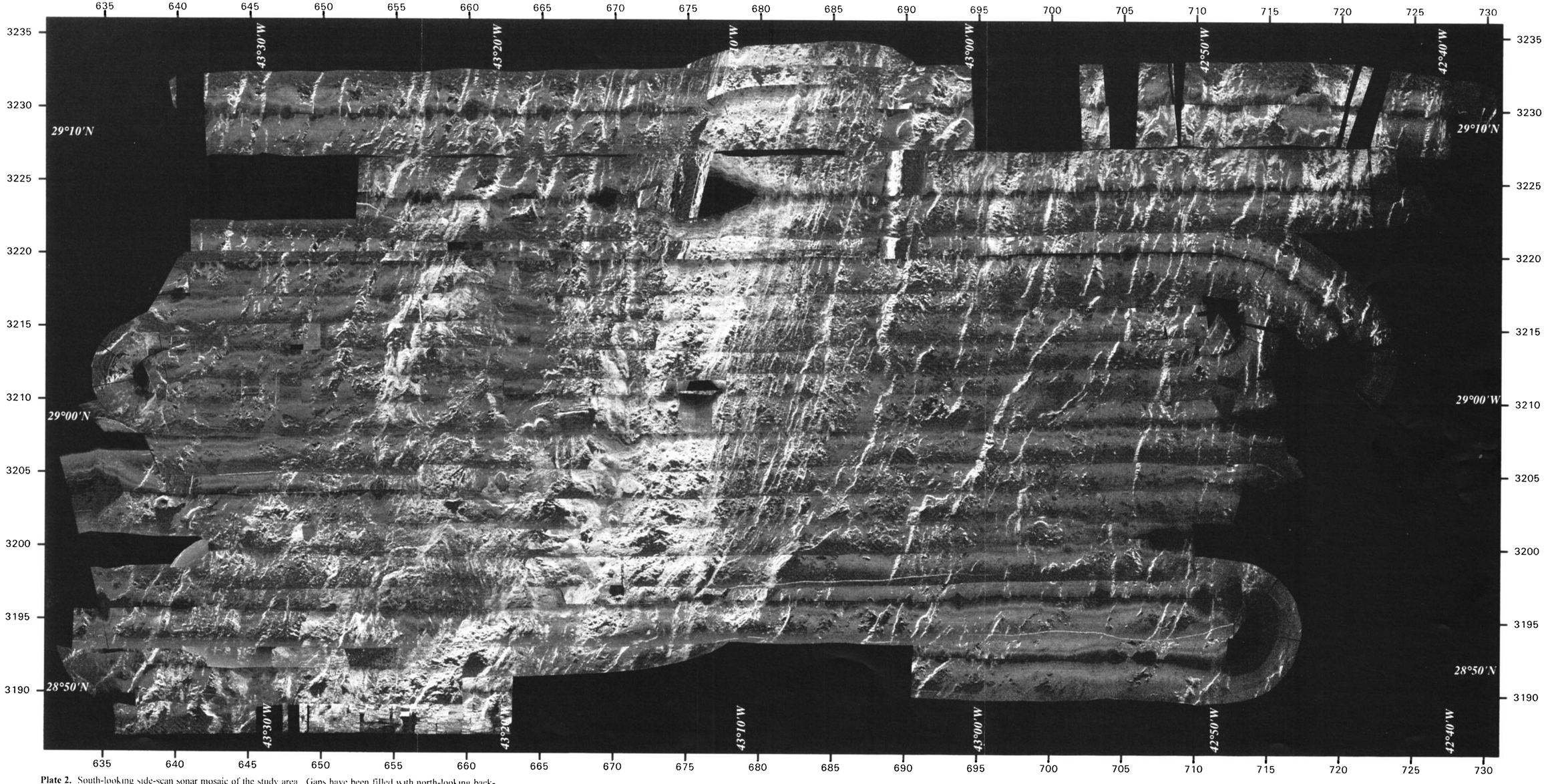

Plate 2. South-looking side-scan sonar mosaic of the study area. Gaps have been filled with north-looking back-scatter data (Plate 2). Other conventions as in Plate 1.

Plates 1 and 2) shows a marked asymmetry (~5 km and ~3 km on the east and west flanks, respectively), consistent with the asymmetric spreading inferred from the deep-tow magnetic profiles (>60% and <40% of the total accretion on the east and west flanks, respectively [*Allerton*, 1997]).

On the east flank small-scale faults can be observed at distances of up to ~15 km off-axis, and the talus of larger faults at distances >20 km appears to be sedimented. These observations indicate that faults are nucleated at ~1-2 km from the axial volcanic ridge and continue to grow to 10-15 km off-axis. Strain only localizes to form larger faults (h>200 m) at >10 km from the axis. These faults may remain active to distances of <20 km off-axis, as indicated by the lack of sediment cover of the talus and scarps. Smaller faults may become inactive between 10 and 20 km off-axis and are not visible off-axis as they are covered by sediments. Faulting at distances <2 km from the axis may occur, but volcanic activity may partially or totally cover faults formed in immediate vicinity of the axial volcanic ridge [see *Macdonald et al.*, 1996].

On the west flank the process of fault formation and strain localization appears to differ substantially from that on the east flank. At the segment end (IC), there is no evidence for a zone of small-scale faulting between the ridge axis and the bounding fault (Figure 3), which has a vertical throw of ~1.5 km (Figure 5). In this case strain localization must occur very close to the ridge axis (<5 km). Most of the tectonic deformation appears to be taken up by this fault, and may inhibiting the formation of small-scale faults. Seismogenic faulting extends to ~10 km off-axis [*Wolfe et al.*, 1995] on the IC, and the backscatter images show at distances <15 km unsedimented fault scarps (i.e., highly reflective scarps with no evidence of a cover of poorly reflective sediments). This observation suggests that faults may be active at <10 km from the ridge axis and become inactive at distances of 10-15 km. Toward the segment center the fault pattern is similar to that of the east flank but with a narrower zone (<10 km) of small-scale faults (i.e., Y=3220-3230 km, X=675 km, Figure 3).

These results indicate that in some cases, such as the IC of this segment, strain may localize very close to the locus of magmatic accretion, resulting in a large rift-bounding wall that accommodates most of the tectonic strain early in the history of the oceanic crust. More generally (east flank and segment center on the west flank), faulting is nucleated over a relatively wide zone (10-15 km), and strain localizes in one or more faults at distances >5 km from the axis. Faults appear to become inactive at 15-20 km off-axis on both flanks, as indicated by the backscatter images, fault distributions, and microseismic activity. The with of this zone is consistent with the ~20-km zone of teleseismic activity reported by *Lin and Bergman* [1990]. These results suggest that the width of active zone is similar on both sides (i.e., ~15-20 km from the ridge axis). At the fast spreading East Pacific Rise (EPR), estimates of the width of the zone of active deformation vary from <10 km [e.g., *Edwards et al.*, 1991] to ~30 km about the ridge axis [e.g., *Alexander and Macdonald*, 1996], with fault spacings of 1-1.4 km [*Edwards et al.*, 1991], and scarp heights of <100 m [*Alexander and Macdonald*, 1996]. The thicker brittle layer at the ridge axis of slow spreading ridges may explain these systematic differences in fault spacing and height between the MAR and the EPR. Although the width of the active zone of deformation is not well constrained at the EPR, at both fast and slow spreading ridges it may be strongly controlled by the thickening of the lithosphere off-axis due to cooling [e.g., *Alexander and Russell*, 1991; *Searle et al.*, 1998b].

6.2. Asymmetric Tectonic Strain

The differences in fault patterns described above indicate a marked E-W asymmetry both in fault characteristics (h and s), and in tectonic strain (ε) that cannot be explained by variations in melt supply along the ridge axis inferred from crustal thickness estimates [e.g., *Lin et al.*, 1990; *Wolfe et al.*, 1995]. The average fault heave increases from ~100 m at the OC to ~400 m at the IC, the spacing from ~1.6 to ~2.6 km (Tables 2 and 3), and the strain from ~7% to ~15% (Table 4 and Figures 9 and 10). A similar pattern but with less asymmetry is observed when the SC-W and SC-E areas are compared (Tables 2-4 and Figure 8). The larger asymmetry observed at the segment end is consistent with that reported in bathymetry and gravity at the segment ends of most slow spreading ridge segments [e.g., *Severinghaus and Macdonald*, 1988; *Tucholke and Lin*, 1994; *Escartín and Lin*, 1995]. However, it is clear that at this segment the asymmetry extends to the segment center.

Part of the asymmetry in tectonic strain may be related to the asymmetry in magmatic accretion inferred from deep-towed magnetic anomalies [*Allerton.*, 1997] (see Figures 8 and 10), which is independent from variations in melt supply along the axis of the segment as inferred from crustal thickness estimates [e.g., *Lin et al.*, 1990; *Wolfe et al.*, 1995]. Magmatic accretion over the last 1 Myr has been highly asymmetric, with 50-150% more accretion on the east than on the west (see location of the central anomaly boundaries at each side of the axis in Figure 8). Cumulative tectonic strain (ε) is proportional to the strain rate ($\dot{\varepsilon}$) and the time length of active tectonic deformation (t) as $\varepsilon = \dot{\varepsilon}/t$. In the case of a mid-ocean ridge, the time length of active deformation of the crust will depend on the width of the zone of deformation (w) and the spreading rate (sr) as t=sr/w. From our observations we assume that the zone of active deformation is of approximately the same width on both sides of the ridge (~15-20 km). Lacking any additional constraints, we also assume that the rate of tectonic deformation is the same on both flanks. In the

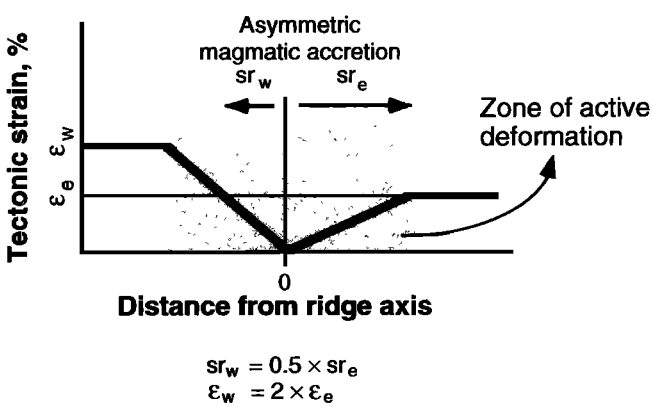

Figure 10. Cartoon showing asymmetric tectonic strain due to asymmetric spreading. The zone of deformation, where faults nucleate and accumulate strain, is relatively symmetric across the axis. We assume that magmatic accretion is asymmetric (for simplicity, ~50% on the west with respect to the east flank) and that the rate of deformation is constant. As the crust on the west flank remains on the zone of deformation during a longer period of time, the final cumulative tectonic strain recorded by the crust will be larger on the west than on the east flank; sr_W and sr_e correspond to the relative spreading rate towards the west and east, respectively; ε_W and ε_r correspond to the cumulative tectonic strain on the west and east flank, respectively.

case of the 29°N segment, if the accretion on the west is ~50% of that on the east, the observed tectonic strain on the west will then be approximately double of that on the east (Figure 10), which is qualitatively consistent with our observations.

Macdonald and Luyendyk [1977] showed that at 37°N there is an inverse relationship between the sense of asymmetry and the amount of tectonic extension. Spreading rate to the west is ~50% of that to the east (7 versus 13 km/Myr), but tectonic strain on the west is ~60% smaller than on the east (11% versus 18%) [*Macdonald and Luyendyk*, 1977]. These discrepancies between the results from both study areas could be due to variations in some of the unconstrained parameters. In particular, at 37°N differences in the width of the active zone of deformation and/or the rate of deformation between the east and the west flanks could result relationships between accretion and tectonic strain that differ from those at 29°N. Additional constraints on these parameters may be obtained with studies on areas to determine the local variations in tectonic strain and fault patterns and their relationship with the asymmetry in plate accretion.

6.3. Partitioning Tectonic Strain and Magmatic Accretion at the Segment Scale

Tectonic strain along the 29°N segment does not vary substantially in an axis-parallel direction. Although the IC shows the largest cumulative tectonic strain, the average strain at the segment end (IC and OC) is only marginally smaller than at the segment center (SC-W and SC-E, ~12% versus ~11%, respectively). Tectonic strain observed at the seafloor in the study area is found to be constant at ~10%, about twice larger than that reported for the East-Pacific Rise [e.g., *Cowie et al.*, 1993; *Alexander and Macdonald*, 1996]. This implies that ~90% of the total plate separation must be accommodated by magmatic processes. Residual gravity anomalies indicate that the crustal thickness along the ridge axis decreases from ~7.5 km at the segment center (-30 mGal mantle Bouguer anomaly) to ~4 km (~-10 mGal) at the segment end [*Lin et al.*, 1990], suggesting that magmatic accretion is highly focused [*Lin et al.*, 1990], and that melt supply at the end of segment is ~50% of that at the segment center. If peridotites are present at the ends of the segment [*Cannat et al.*, 1995; *Cannat*, 1996], the geophysically defined crustal thickness may overestimate the actual magmatic crustal thickness, and variations in melt supply along the segment may be even larger. Small along-axis variations in magmatic accretion (e.g., from 90% to 70% of the total plate separation) associated with variations in melt supply would result in a three-fold (10% to 30%) increase in tectonic strain (Figure 11). Such large variation in tectonic strain should be recognizable based on the estimates of tectonic strain deduced from the data analysis presented here, as it would result in very large variations in fault spacing, heave and/or geometry that are not observed in this area.

These results suggest that, in shallow levels of the oceanic lithosphere, tectonic strain is decoupled from magmatic processes. This decoupling occurs at time-scales of ~1 Myr over

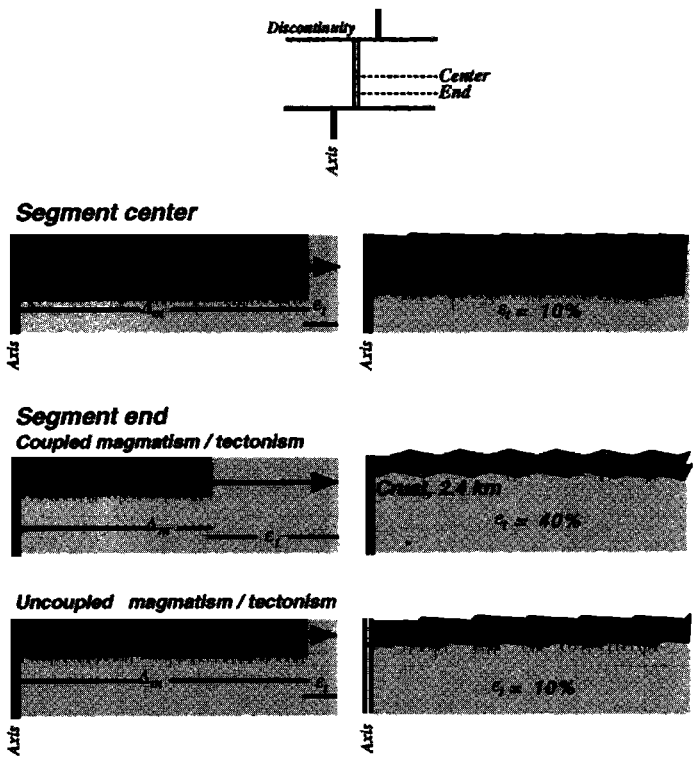

Figure 11. Cartoon showing the difference between tectonic strain coupled and uncoupled with melt supply to the axis. ε_t corresponds to tectonic strain, and Δ_m corresponds to magmatic accretion. Total plate separation is $\varepsilon_t+\Delta_m$ (left), tectonic strain is assumed to be taken up by brittle faulting (right; geometry of faults shown is unconstrained and for illustration purposes only). The thickness of the crust at the ridge axis decreases from ~7 km at the segment center to ~4 km at the end [*Lin et al.*, 1990]. Tectonic strain averages ~10%, both at the center and end of segment (top and bottom). If melt supply (i.e., crustal thickness) were directly linked to tectonic processes (center) we would expect the tectonic strain ε_t at the segment end to be substantially larger than at the center. This is not supported by the data. See text for discussion.

which we have estimated tectonic strain, and over the length of an individual ridge segment. Thus variations in crustal thickness along the axis of slow spreading segments [e.g., *Lin et al.*, 1990; *Tolstoy et al.*, 1993; *Detrick et al.*, 1995; *Cannat*, 1996] may reflect variations in melt supply but do not imply variations in tectonic strain. As tectonic thinning of the crust can be important off-axis [e.g., *Escartín and Lin*, 1995; 1998], crustal thickness estimates at these locations cannot be used to infer temporal variations in magma supply or tectonic strain. In depth the accommodation of the plate separation among tectonic extension and magmatic accretion may vary substantially. Possible processes operating at the base of the lithosphere may include passive accretion of asthenospheric material into the lithosphere as the plates separate [*Cannat*, 1996] and distributed brittle processes, in addition to localized brittle deformation. Identification and quantification of both passive accretion of asthenospheric material and/or distributed deformation require further geological constraints, and cannot be done from the sea surface bathymetric of backscatter data presented here.

Fault spacing and heave change substantially along axis even though tectonic strain is relatively constant. For example, fault heave at the west flank decreases from ~400 m (segment end, IC) to ~250 m (segment center, west, Table 2 and Figure 10), and fault spacing decreases from ~2.6 to ~1.5 km (also from end to center, Table 3 and Figure 10). As these changes in fault characteristics do not correlate with the estimated long-term tectonic strain, we infer that they are due instead to changes in rheology induced by the thickening of the lithosphere toward the segment ends [*Forsyth*, 1992; *Shaw*, 1992], by the weakening of fault planes [*Escartín et al.*, 1997b] due to the presence of serpentinized materials along shear zones [e.g., *Francis*, 1981], or by the combination of both effects. Lithospheric thickening toward segment ends has been invoked to explain tectonic patterns observed near discontinuities [e.g., *Fox and Gallo*, 1984], but thermal models of nontransform discontinuities [e.g., *Parmentier and Forsyth*, 1985; *Shaw and Lin*, 1996] only predict small changes in the depths to isotherms. In addition, changes in fault spacing and heave may be more sensitive to the rheology of the oceanic lithosphere and faults than to its thickness [*Escartín et al.*, 1997b]. Serpentinites and gabbros have been dredged at the base of the large fault scarp bounding the west flank of the rift valley at the segment end [*Cann et al.*, 1997; *CD99 Scientific Party*, 1996] (Figure 3), suggesting that the crust at the IC may be heterogeneous. Owing to the weak nature of serpentinites [e.g., *Reinen et al.*, 1994; *Escartín et al*, 1997a] their presence may greatly enhance strain localization along fault planes, resulting both in larger displacements and increased fault spacings [*Escartín et al.*, 1997b].

6.4. Formation of Outward Facing Faults

Outward facing faults in our study area represent <10% of the total number of faults and account for a small proportion of the total tectonic strain. While at 23°N and 37°N this proportion is estimated to be ~20% [*Kong et al.*, 1988; *Macdonald and Luyendyk*, 1977], in an adjacent area at 25.5°-27.2°N, *Jaroslow* [1996] reports that ~40% of the total fault population correspond to outward-facing faults. This proportion of outward-facing faults reported by *Jaroslow* [1996] is similar to that given for fast spreading ridges [see *Carbotte and Macdonald*, 1990, and references therein]. *Jaroslow*'s [1996] study, based on the interpretation of shipboard multibeam bathymetry and HMR1 backscatter data, shows that the proportion of outward facing faults increases from ~10% at the ridge axis to ~40% at ~3 Ma old crust and remains relatively constant out to 20 Ma off-axis. This result is not consistent with the fault patterns in our study area, as we observe no evidence for an increase of the number of outward facing faults towards the east and west limits of the survey area (~3 Ma, Figures 1 and 3). If a similar process of formation of outward-facing faults operates at the 29°N segment, it must occur at seafloor ages older than 3 Ma, outside of our survey area. Alternatively, some of the outward facing faults interpreted by *Jaroslow* [1996] may not be properly constrained due to the coarser resolution of the multibeam bathymetry and HMR1 backscatter data. They may correspond instead to volcanic terrain backtilted by flexural rotation caused inward facing faults, as seen in some areas at the 29°N segment. Analyses of coincidental high-resolution TOBI data, multibeam bathymetry, and HMR1 backscatter data would be required to unequivocally determine the nature of these features and to establish if the formation and tectonic evolution of outward facing faults are operating farther off-axis at the 29°N segment.

7. Conclusions

We have presented the results of a comprehensive analysis of fault data interpreted from high-resolution side-scan sonar imagery covering two-thirds of the length of a slow spreading segment, extending out to ~3 Ma old crust. These results reveal that changes in fault patterns and tectonic strain are not correlated. The zone of active deformation is estimated to extend to ~10-20 km off-axis, and may be controlled by the thermal structure below the ridge. We infer that variations in fault spacing and heave are controlled primarily by changes in the rheology of faults, and secondarily by changes in lithospheric thickness. These results indicate that the amount of tectonic strain is not the primary control on the development of faults. The major conclusions of this study are as follows:

1. Approximately 10% of the total strain observed at the seafloor is accommodated by brittle faulting. The rest of the plate separation (90%) must be taken up by either magmatic accretion or diffuse tectonic deformation within the crust without an expression on the seafloor surface. Estimates of apparent tectonic strain are an upper bound of the actual tectonic strain.

2. Outward facing faults are scarce and account for <10% of the total number of faults and tectonic strain.

3. Variations in tectonic strain cannot be resolved along the axis and show no correlation with changes in melt supply as inferred from changes in crustal thickness along the axis.

4. We observe a marked asymmetry in tectonic strain of up to 50% between the east and west flanks, both at the segment center and end. Asymmetric strain maybe partially explained by the asymmetric magmatic accretion at the axis documented by near-bottom magnetic profiles.

5. Differences in fault geometry (heave and spacing) among different regions of the segment are not directly correlated with total tectonic strain but instead may reflect changes in lithospheric rheology (thickness, composition). Our study corroborates that faults are largest and have the widest spacing at the IC, while faults at the OC are smaller. An increase in fault size and spacing is observed from the segment center toward the ends, while tectonic strain remains constant. These variations in fault geometry may be better explained by rheological changes along fault planes associated with the presence of weak serpentinites, as changes in lithospheric thickness along a segment predicted by thermal models are not very important.

Acknowledgments. We thank the officers and crew of the RRS *Charles Darwin* cruise CD99 and the TOBI team for their assistance. We thank Mathilde Cannat, Gary Jaroslow, Jian Lin, Debbie Smith and Brian Tucholke for discussions and comments that contributed to the ideas presented in the paper. Thorough reviews by R. L. Carlson, D. Fornari and K. C. Macdonald helped clarify our arguments and improve our manuscript The GMT software [*Wessel and Smith*, 1991] was extensively used in this study. Funding for this work was provided by the National Research Council (UK).

References

Alexander, R. T., and K. C. Macdonald, SeaBeam, SeaMARCII and Avin-based studies of faulting on the East Pacific Rise 9°20'N-9°50'N, *Mar Geophys Res*, *18*, 557-587, 1996.

Allerton, S., R. C. Searle and B. J. Murton, Bathymetric segmentation and faulting on the Mid-Atlantic Ridge, 24°00'N to 24°40'N, in *Tectonic, Magmatic, Hydrothermal and Biological Segmentation of Mid-Ocean Ridges*, edited by C. J. MacLeod, T. A. Tyler and C. L. Walker, *Geol. Soc. Spec. Publ.*, *118*, 29-48, 1996

Allerton, S., Evidence for asymmetric accretion at the end of a slow-spreading segment (abstract), *Eos, Trans. AGU*, *78*, F692, 1997.

Cann, J. R., D. K. Blackman, D. K. Smith, E. McAllister, B. Janssen, S. Mello, E. Avgerinos, A. R. Pascoe, and J. Escartin, Corrugated slip surfaces formed at North Atlantic ridge-transform intersections, *Nature*, *385*, 329-332, 1997.

Cannat, M., Emplacement of mantle rocks in the seafloor at mid-ocean ridges, *J. Geophys. Res*, *98*, 4163-4172, 1993

Cannat, M., How thick is the magmatic crust at slow spreading oceanic ridges?, *J. Geophys. Res.*, *101*, 2847-2857, 1996.

Cannat, M., C Mével, M. Maia, C. Deplus, C. Durand, P. Gente, P. Agrinier, A. Belarouchi, G. Dubuisson, E. Humler, and J. Reynolds, Thin crust, ultramafic exposures, and rugged faulting patterns at the Mid-Atlantic Ridge (22°-24°N), *Geology*, *23*, 49-52, 1995.

Carbotte, S., and K. C. Macdonald, Causes of variation in faulting-facing direction on the ocean floor, *Geology*, *18*, 749-752, 1990

Carbotte, S., and K. C. MacDonald, Comparison of tectonic fabric at intermediate, fast, and super fast spreading ridges: Influence of spreading rate, plate motions, and ridge segmentation on fault patterns, *J Geophys Res.*, *99*, 13609-13631, 1994.

CD99 Scientific Party, Near-bottom geophysical studies of the Broken Spur spreading segment, Mid-Atlantic Ridge 29°N, *RRS Charles Darwin Cruise Rep. CD99*, 62 pp, Univ. of Durham, Durham, England, 1996.

Cowie, P. A., and C. H Scholz, Displacement-length scaling relationship for faults· Data synthesis and discussion, *J. Struct. Geol.*, *14*, 1149-1156, 1992.

Cowie, P. A., C. H Scholz, M. Edwards, and A. Malinverno, Fault strain and seismic coupling on mid-ocean ridges, *J Geophys. Res*, *98*, 17911-17920, 1993.

Cowie, P. A., A. Malinverno, W. B F. Ryan, and M H Edwards, Quantitative fault studies on the East Pacific Rise: A comparison of sonar imaging techniques, *J Geophys. Res*, *99*, 15205-15218, 1994.

Dawers, N. H, M. H Anders, and C. H Scholz, Growth of normal faults: Displacement-length scaling, *Geology*, *21*, 1107-1110, 1993.

DeMets, C., R. G. Gordon, D. F Argus and S Stein, Current plate motions, *Geophys. J. Int.*, 101, 425-478, 1990.

Detrick, R. S., H. D. Needham, and V Renard, Gravity anomalies and crustal thickness variations along the Mid-Atlantic Ridge between 33°N and 40°N, *J. Geophys Res.*, *100*, 3767-3787, 1995.

Edwards, M H., D. J. Fornari, A Malinverno, W. B. F Ryan, and J Madsen, The regional tectonic fabric of the East Pacific Rise form 12°50'N to 15°10'N, *J. Geophys. Res.*, *96*, 7995-8017, 1991.

Escartín, J., Ridge segmentation, tectonic evolution and rheology of slow-spreading crust, Ph.D. thesis, 232 pp., MIT/WHOI Joint Program, Woods Hole, Mass., 1996.

Escartín, J., and J. Lin, Ridge offsets, normal faulting, and gravity anomalies of slow spreading ridges, *J. Geophys. Res.*, *100*, 6163-6177, 1995.

Escartín, J., and J. Lin, Tectonic modification of axial crustal structure: Evidence from spectral analyses of residual gravity and bathymetry of the Mid-Atlantic Ridge flanks, *Earth Planet. Sci. Lett.*, *154*, 279-293, 1998.

Escartín, J , G. Hirth, and B. Evans, Non-dilatant brittle deformation of serpentinites· Implications for Mohr-Coulomb theory and the strength of faults, *J. Geophys. Res.*, *102*, 2897-2913, 1997b.

Escartín, J., G. Hirth, and B. Evans, Effects of serpentinization on the lithospheric strength and the style of normal faulting at slow-spreading ridges, *Earth Planet. Sci. Lett.*, *151*, 181-190, 1997a.

Flewellen, C., N. C. Millard and I. Rouse, TOBI, a vehicle for deep ocean survey, *Elect. Commun. Eng. J.*, *22*, 85-93, 1993.

Forsyth, D. W., Finite extension and low-angle normal faulting, *Geology*, *20*, 27-30, 1992.

Fox, P. J., and D. G. Gallo, A tectonic model for ridge-transform-ridge plate boundaries· Implications for the structure of oceanic lithosphere, *Tectonophysics*, *104*, 205-242, 1984.

Francis, T. J. G., Serpentinization faults and their role in the tectonics of slow spreading ridges, *J. Geophys. Res.*, *86*, 11616-11622, 1981.

Goff, J. A., and B. E. Tucholke, Multiscale spectral analysis of bathymetry on the flank of the Mid-Atlantic Ridge: Modification of the seafloor by mass wasting and sedimentation, *J. Geophys. Res*, *102*, 15447-15462, 1997.

Goff, J. A., B. E Tucholke, J. Lin, G. E. Jaroslow, and M. C Kleinrock, Quantitative analysis of abyssal hills in the Atlantic Ocean: A correlation between axis crustal thickness and extensional faulting, *J. Geophys. Res.*, *100*, 22509-22522, 1995.

Goff, J. A., Y. Ma, A. Shah, J. R Cochran, and J.-C. Sempéré, Stochastic analysis of seafloor morphology on the flank of the Southeast Indian Ridge: The influence of ridge morphology on the formation of abyssal hills, *J Geophys. Res*, *102*, 15521-15534, 1997.

Hussenoeder, S. A., M A. Tivey, and H. Schouten, Direct inversion of potential fields from an uneven track with application to the Mid-Atlantic Ridge, *Geophys Res Lett.*, *22*, 3131-3134, 1995.

Jaroslow, G. E., The geological record of oceanic crustal accretion and tectonism at slow-spreading ridges, Ph.D. Thesis, 210 pp., MIT/WHOI Joint Program, Woods Hole, Mass., 1996

Kong, L. S., R. S. Detrick, P. J. Fox, L. A. Mayer, and W. B. F. Bryan, The morphology and tectonics of the MAR area from Sea Beam and Sea MARC I observations (Mid-Atlantic Ridge 23°N), *Mar Geophys. Res.*, *10*, 59-90, 1988.

Kuo, B. Y., and D. W. Forsyth, Gravity anomalies of the ridge-transform system in the South Atlantic between 30° and 31°S: Upwelling centers and variations in crustal thickness, *Mar. Geophys. Res.*, *10*, 205-232, 1988.

Laughton, A. S, R. C. Searle, and D. G. Roberts, The Reykjanes ridge crest and the transform between its rifted and non-rifted regions, *Tectonophysics*, *55*, 173-177, 1979.

le Bas, T. P., D. C. Mason, and N C. Millard, TOBI image processing-The state of the art, *IEEE J. Ocean Eng.*, *20*, 85-93, 1995.

Lin, J., and E. A. Bergman, Rift grabens, seismicity and volcanic segmentation of the Mid-Atlantic Ridge: Kane to Atlantis Fracture Zones (abstract), *Eos, Trans. AGU*, *71*, 1572, 1990.

Lin, J., G. M. Purdy, H. Schouten, J. C. Sempéré, and C. Zervas, Evidence from gravity data for focused magmatic accretion along the Mid-Atlantic Ridge, *Nature*, *344*, 627-632, 1990

Macdonald, K. C., and B. P. Luyendyk, Deep-Tow studies of the structure of the Mid-Atlantic Ridge crest near lat 37°N, *Geol Soc Amer. Bull*, *88*, 621-636, 1977.

Macdonald, K. C., P. J. Fox, R T. Alexander, R. Pockalny, and P. Gente, Volcanic growth faults and the origin of Pacific abyssal hills, *Nature*, *380*, 125-129, 1996.

McAllister, E., and J R. Cann, Initiation and evolution of boundary-wall faults along the Mid-Atlantic Ridge, 25-29°N, in *Tectonic, Magmatic, Hydrothermal and Biological Segmentation of Mid-Ocean Ridges*, edited by C. J. MacLeod, T. A. Tyler and C. L Walker, *Geol Soc Spec. Publ*, *118*, 29-48, 1996.

McAllister, E., J. Cann, and S. Spencer, The evolution of crustal deformation in an oceanic extensional environment, *J. Struct. Geol*, *17*, 183-199, 1995.

Murton, B. J., C. Van Dover and E. Southward, geological setting and ecology of the Broken Spur hydrothermal vent field· 29.1°N on the Mid-Atlantic Ridge, *Hydrothermal vents and processes*, edited by L. M. Parson, C. L. Walker, and D. R. Dixon, *Spec Publ. Geol Soc. London*, *87*, 33-41, 1995.

Pariso, J. E, J.-C Sempéré, and C Rommeveaux, Temporal and spatial variations in crustal accretion along the Mid-Atlantic Ridge (29°-31°31'N) over the last 10 Myr: Implications from a three-dimensional gravity study, *J. Geophys. Res.*, *100*, 17781-17794, 1995.

Parmentier, E. M., and D. W. Forsyth, Three-dimensional flow beneath a slow spreading ridge axis: A dynamic contribution to the deepening of the median valley toward fracture zones, *J. Geophys. Res*, *90*, 678-684, 1985.

Purdy, G. M., J. C. Sempéré, H. Schouten, D. L. Dubois, and R. Goldsmith, Bathymetry of the Mid-Atlantic Ridge, 24°-31°N: A map series, *Mar. Geophys. Res.*, *12*, 247-252, 1990.

Reinen, L. A., J. D. Weeks, and T. E. Tullis, The frictional behavior of lizardite and antigorite serpentinites: Experiments, constitutive models, and implications for natural faults, *Pure Appl. Geophys.*, *143*, 318-358, 1994.

Rommeveaux, C., C. Deplus, P. Patriat, and J.-C. Sempéré, Three-dimensional gravity study of the Mid-Atlantic Ridge: Evolution of the segmentation between 28° and 29°N during the last 10 m.y., *J. Geophys. Res.*, *99*, 3015-3029, 1994.

Sandwell, D. T., and W. H. F. Smith, Marine gravity anomaly from Geosat and ERS1 satellite altimetry, *J. Geophys. Res.*, *102*, 10039-10054, 1997.

Searle, R. C., and A S. Laughton, Fine-scale sonar study of tectonics and volcanism of the Reykjanes Ridge, *Oceanologica Acta*, *4*, 5-13, 1981.

Searle, R. C., P. A. Cowie, N. C. Mitchell, N. C. Allerton, C. J. MacLeod, J. Escartín, S. M. Russell, P. A. Slootweg, and T. Tanaka, Detailed evolution of a slow spreading ridge segment: the Mid-Atlantic Ridge at 29°N, *Earth Planet. Sci Lett*, *154*, 167-183, 1998a.

Searle, R. C., J. A. Keeton, R. B. Owens, R. S. White, R. Mecklenburgh, B. Parsons, and S. M. Lee, The Reykjanes Ridge: Structure and tectonics of a hot-spot-influenced slow-spreading ridge, from multibeam bathymetry, gravity and magnetic investigations, *Earth Planet. Sci. Lett*, *160*, 463-478, 1998b.

Sempéré, J.-C., J. Lin, H. S. Brown, H. Schouten, and G. M. Purdy, Segmentation and morphotectonic variations along a slow-spreading center: The Mid-Atlantic Ridge (24°N - 30°30'N), *Mar. Geophys Res.*, *15*, 153-200, 1993.

Sempéré, J.-C., P. Blondel, P. Briais, T. Fujiwara, L. Géli, N. Isezaki, J. E. Pariso, L. Parson, P. Patriat, and C. Rommevaux, The Mid-Atlantic Ridge between 29°N and 31°30'N in the last 10 Ma, *Earth Planet Sci. Lett.*, *130*, 45-55, 1995.

Severinghaus, J. P., and K. C. MacDonald, High inside corners at ridge-transform intersections, *Mar. Geophys. Res.*, *9*, 353-367, 1988.

Shaw, P. R., Ridge segmentation, faulting and crustal thickness in the Atlantic Ocean, *Nature*, *358*, 490-493, 1992.

Shaw, P. R., and J. Lin, Causes and consequences of variations in faulting style at the Mid-Atlantic Ridge, *J. Geophys. Res.*, *98*, 1839-21851, 1993.

Shaw, W. J., and J. Lin, Models of ocean ridge lithospheric deformation: Dependence on crustal thickness, spreading rate, and segmentation, *J. Geophys. Res.*, *101*, 17977-17993, 1996.

Smith, D. K., J. R. Cann, M. E. Dougherty, J. Lin, S. Spencer, C. MacLeod, J. Keeton, E. McAllister, B. Brooks, R Pascoe, and W. Robertson, Mid-Atlantic Ridge volcanism from deep-towed side-scan sonar images, 25°-29°N, *J. Volcanol. Geotherm. Res*, *67*, 233-262, 1995.

Solomon, S. C., P. Y. Huang, and L. Meinke, The seismic moment budget of slowly spreading ridges, *Nature*, *334*, 58-60, 1988.

Thatcher, W., and D. P. Hill, A simple model for the fault-generated morphology of slow spreading mid-ocean ridges, *J. Geophys. Res.*, *100*, 561-570, 1995

Tolstoy, M., A. J. Harding, and J. A. Orcutt, Crustal thickness on the Mid-Atlantic Ridge: Bull's eye gravity anomalies and focused accretion, *Science*, *262*, 726-729, 1993.

Triantafyllou, M. S., and F. S. Hover, Cable dynamics for tethered underwater vehicles, *MIT SeaGrant College Program Rep. 90-4*, Mass. Inst. Technol., Cambridge, Mass., 1990.

Tucholke, B. E., and J. Lin, A geological model for the structure of ridge segments in slow spreading ocean crust, *J. Geophys. Res.*, *99*, 11937-11958, 1994.

Tucholke, B E, W. K. Stewart, and M. C. Kleinrock, Long-term denudation of ocean crust in the central North-Atlantic Ocean, *Geology*, *25*, 171-174, 1997.

Wessel, P., and W. H. F. Smith, Free software helps map and display data, *Eos Trans. AGU*, *72*, 445-446, 1991.

Wolfe, C., G. M. Purdy, D. R. Toomey, and S C. Solomon, Microearthquake characteristics and crustal velocity structure at 29°N of the Mid-Atlantic Ridge: The architecture of a slow spreading segment, *J Geophys Res*, *100*, 24449-24472, 1995.

S. Allerton, Robertson Research International, Llandudno LL30 1SA, Wales.

P. A. Cowie, Department of Geology and Geophysics, University of Edinburgh, West Mains Road, Edinburgh EH9 3JW, Scotland

J. Escartín, Laboratoire de Pétrologie, Université Pierre et Marie Curie (Tour 26, 3ème ét., caise 110), 4 Place Jussieu, 75252 Paris Cedex 05, France. (email: escartin@ccr.jussieu.fr)

C. J. MacLeod, Department of Earth Sciences, University of Wales Cardiff CF1 3YE, Wales

N C. Mitchell, Department of Earth Sciences, University of Oxford, Parks Road, Oxford OX1 3PR, England.

R. C. Searle and A. P. Slootweg, Department of Geological Sciences, South Road, Durham DH1 3LE, England.

(Received April 1, 1998; Revised September 29, 1998;
accepted November 23, 1998)